Stress distribution and development within geosynthetic-reinforced soil slopes

K.-H. Yang[1], J. G. Zornberg[2], C.-N. Liu[3] and H.-D. Lin[4]

[1]*Assistant Professor, Department of Construction Engineering, National Taiwan University of Science and Technology, 43, Sec. 4, Keelung Rd., Taipei 106, Taiwan, Telephone: +886 2 2730 1227, Telefax:+886 2 2737 6606, E-mail: khy@mail.ntust.edu.tw*
[2]*Associate Professor, Department of Civil, Architectural and Environmental Engineering, University of Texas at Austin, 1 University Station C1792, Austin, TX 78712, USA, Telephone: +1 512 232 3595, Telefax: +1 512 471 6548, E-mail: zornberg@mail.utexas.edu*
[3]*Professor, Department of Civil Engineering, National Chi Nan University, No. 1, University Rd, Puli, Nantou County, 545 Taiwan, Telephone: +886 49 2910 960 ext. 4958, Telefax: +886 49 2918 679, E-mail: cnliu@ncnu.edu.tw*
[4]*Professor, Department of Construction Engineering, National Taiwan University of Science and Technology, 43, Sec. 4, Keelung Rd., Taipei 106, Taiwan, Telephone: +886 2 2737 6559, Telefax:+886 2 2737 6606, E-mail: hdlin@mail.ntust.edu.tw*

Received 21 November 2010, revised 22 September 2011, accepted 2 December 2011

ABSTRACT: Numerical methods combined with centrifuge tests are used to investigate the distribution and development of soil stresses and reinforcement tensile loads in geosynthetic-reinforced soil (GRS) structures. In this study, system stability indicated by the factor of safety (FS) of GRS slopes is calculated by limit equilibrium analysis. Stress information under various stress states is evaluated using finite element analysis. Advanced models and an integration algorithm are implemented in finite element code to enhance the simulation results. The proposed numerical models are validated by centrifuge tests of two GRS slopes with different backfill densities. Numerical results indicate that soil stress mobilisation can be described by the soil stress level S, which is defined as the ratio of the current stress status to peak failure criteria. For both slope models, as loading increases, backfill stresses develop and propagate along the potential failure surface. Mobilisation of soil stress was non-uniform along the failure surface. Immediately after the stress level reaches peak ($S = 1$), strength softening initiates at the top and toe of the slope at approximately FS = 1.2. The slope settlement rate and reinforcement tensile load increase significantly when soil softening begins. The softening occurs randomly and irregularly along the failure surface, and the formation of the soil-softening band completes at approximately FS = 1.1. The failure surface corresponds to the locus of intense soil strains and the maximum tensile loads at each reinforcement layer. Additionally, the numerical results show that the initiation of soil softening and the failure of the slope occurred earlier in the slope model with low backfill density. The numerical results support the view that peak shear strength, not residual shear strength, governs system stability. Last, the distribution of maximum reinforcement tensile loads with depth was highly uniform at low g-level and became trapezoidal at high g-level. The peak value was located at approximately mid-height of the reinforced slopes. This observation contradicted the triangular distribution with depth assumed in current design methodologies for geosynthetic structures.

KEYWORDS: Geosynthetics, Geosynthetic-reinforced soil structures, Stress distribution and development, Finite element analysis, Centrifuge test

REFERENCE: Yang, K.-H., Zornberg, J. G., Liu, C.-N. & Lin, H.-D. (2012). Stress distribution and development within geosynthetic-reinforced soil slopes. *Geosynthetics International*, **19**, No. 1, 62–78. [http://dx.doi.org/10.1680/gein.2012.19.1.62]

1. INTRODUCTION

The information of backfill stresses and reinforcement tensile loads within geosynthetic-reinforced soil (GRS) structures offers an important insight into the basis of design. This information can be applied to examine the design methodologies in current design guidelines (Elias *et al.* 2001; AASHTO 2002; NCMA 2010). One example is conservative prediction of reinforcement loads when using current design methods (Allen and Bathurst 2002a, 2002b; Allen *et al.* 2003; Bathurst *et al.* 2008). This information is also useful for decision-making in current designs, such as selecting peak or residual soil shear strength properties for design (Leshchinsky 2001; Zornberg and Leshchinsky 2001; Zornberg 2002a, 2002b, 2002c, 2002d, 2003).

However, because of the complex interaction between soil and reinforcement, these data, particularly backfill stress, have not been satisfactorily elucidated, mainly because current physical and numerical methods are inadequate. Physical methods such as in situ monitoring and full-scale tests typically use pressure cells to measure soil pressure. However, adjusting pressure cells in the direction of interest (e.g. soil stress along the failure surface) after installation is difficult. Additionally, pressure cells can only measure the soil normal stresses in the direction perpendicular to the plane of pressure cells. Stress information on the two planes orthogonal to the plane of pressure cells and the shear stresses are unobtainable. Small-scale models used in centrifuge tests also raise concerns that intrusive instrumentation may disturb the development of soil stresses. Numerical simulations provide limited useful data on soil stress and strain. For example, although the finite element method satisfactorily models conservatively designed GRS structures under working stress conditions, it is inadequate for predicting the behaviour of GRS structures under large deformation conditions. This problem arises because most constitutive soil models do not consider the post-peak behaviour of the soil. This is a crucial problem when evaluating soil stresses under large soil strain conditions (3–5% for typical granular soils), especially in comparatively flexible structures such as GRS structures. Numerical accuracy and stability are particularly important in the post-peak region of the soil.

The above observations prompt the current study of stress information within GRS structures. The objective is to characterise the distribution and development of backfill stresses and reinforcement tensile loads within GRS structures by combining several methods. The factor of safety of GRS slopes, which is calculated by limit equilibrium analysis, is used as an indicator of system stability. The mobilisation of soil stresses and reinforcement tensile loads under various soil stress states is evaluated by finite element analysis. Advanced soil and reinforcement models and an integration algorithm are implemented into the finite element code in order to better simulate the behaviour of GRS structures under large soil strain or near-failure conditions. The proposed numerical models are validated by centrifuge testing of two GRS slopes with different backfill densities. The stress data obtained by the numerical simulations are useful for interpreting the behaviour of GRS structures, and offer valuable insights into the design of GRS structures.

2. CENTRIFUGE TESTS AND LIMIT EQUILIBRIUM ANALYSES

2.1. Centrifuge tests

Arriaga (2003) performed a series of centrifuge tests to investigate the response of GRS slopes under various stress states. Two of these centrifuge tests, Models M1 and M3, were selected for analysis in this study. They have similar dimensions and reinforcement layouts, but different backfill relative densities ($D_r = 70\%$ and 50%, respectively). Figure 1a shows a photograph of the centrifuge slope model, and Figure 1b illustrates the geometric configuration of the two models. The geotextile-reinforced structures were 228 mm high and built on a foundation layer 25 mm thick. The slope models were 254 mm high in total. The geotextile was 203 mm long with 25.4 mm vertical spacing. The geotextile was folded back to form a wrap-around facing and a secondary (overlapping) layer (length 50 mm).

Table 1 shows the properties of the Monterey No. 30 sand used as the backfill and foundation material. The backfill unit weight and friction angle obtained from a series of triaxial compression tests were $\gamma = 16.0$ kN/m^3 and $\phi_{tc} = 36.7°$ at $D_r = 70\%$, and $\gamma = 15.7$ kN/m^3 and $\phi_{tc} = 34.7°$ at $D_r = 50\%$. The estimated plane-strain friction angles reported in Zornberg *et al.* (1998b) were $\phi_{ps} = 42.2°$ and 39.1°.

The reinforcement material used in the centrifuge study was Pellon Sew-in, a commercially available nonwoven interfacing fabric. The average unconfined tensile strength from wide-width tensile tests was $T_{ult\_uncomfined} = 0.03$ kN/m. Although the wide-width tensile test is widely used to determine the tensile strength of geotextiles, the results provided by unconfined testing are not representative of the actual conditions in centrifuge tests. It has been reported that the ultimate tensile strength increases under confinement (Leshchinsky and Field 1987). The strength increase probably results not only from soil confinement, but also from the interaction between soil particles in contact with geotextile fibres (Montalvo and Sickler 1993). Back-calculation of slope failure using limit equilibrium analyses showed that the average value of ultimate confined tensile strength for this geotextile was $T_{ult\_confined} = 0.124$ kN/m, which is approximately fourfold higher than the ultimate unconfined tensile strength. The back-calculation analyses used to obtain the ultimate confined tensile strength of reinforcement are discussed further in Section 2.2.

Figure 2 shows a series of in-flight screenshots taken when Model M1 was subjected to increased centrifugal force (or *g*-level). Each slope model was loaded to failure, which was indicated by a large settlement measured by an LVDT located at 38.1 mm from the front crest of slope. The recorded failure *g*-levels for Models M1 and M3 were 50*g* and 36*g*, respectively.

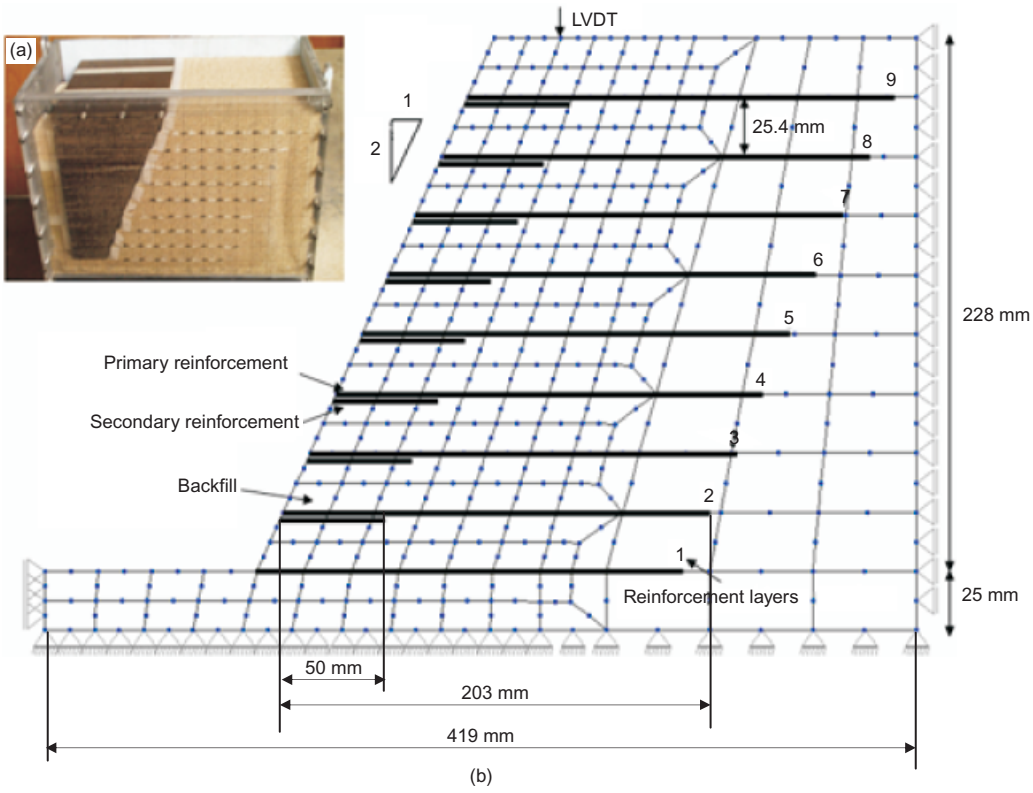

Figure 1. Configuration of Models M1 and M3: (a) centrifuge model; (b) FE mesh

Table 1. Properties of Monterey No. 30 sand

Property	Value
D_{50} (mm)	0.4
Uniformity coefficient, C_u	3
Coefficient of curvature, C_c	1.1
Specific gravity, G_s	2.66
Soil classification	SP
Max. dry unit weight, $\gamma_{d,max}$ (kN/m^3)	16.7
Min. dry unit weight, $\gamma_{d,min}$ (kN/m^3)	14.76

2.2. Limit equilibrium analyses

Limit equilibrium analyses were performed to calculate the factor of safety and to locate the failure surfaces on the GRS slopes. Limit equilibrium calculations were performed using Spencer's method (Spencer 1967), with circular surfaces as coded in the computer program UTEXAS4. The plane-strain friction angle of backfill was used to characterise the shear strength of the Monterey No. 30 sand. The centrifugal force was simulated by increasing the unit weight of the backfill N times corresponding to the target g-level.

The limit equilibrium analyses assumed that the reinforcement forces had a uniform distribution with depth. The analyses considered the contribution of geotextile overlap layers to system stability. Unlike the recommended use of allowable tensile strength in conventional analysis, the limit equilibrium analyses in this study did not consider reduction factors due to installation damage, creep or degradation (i.e. all reduction factors were 1.0). Reduction factors were excluded, because the centrifuge model was carefully constructed to ensure that no installation damage occurred, and the test duration was kept relatively short so that no long-term behaviour such as creep or degradation would occur. The confined tensile strength was considered the ultimate strength when the g-level corresponding to FS = 1 calculated in limit equilibrium analysis equalled the failure g-level observed in each centrifuge test (i.e. 50g for Model M1 and 36g for Model M3). Thus the back-calculated tensile strength was expected to equal the average reinforcement tension at the moment of failure.

In this study, the back-calculated ultimate confined tensile strength of reinforcement was used to estimate the FS of the centrifuge model as the g-level increased so that the FS could be used to indicate system stability. Figure 3 shows the relationships between FS and g-level for Models M1 and M3. The calculated FS generally decreases as g-level increases, which suggests that system stability decreases as loading increases. The failure surfaces identified by the limit equilibrium analysis are compared with those identified by centrifuge tests and finite element simulations. The comparison of failure surface locations is discussed further below.

3. FINITE ELEMENT MODEL

The mobilisation of soil stresses and reinforcement tensile loads under various stress states was evaluated using finite element analyses. Finite element modelling was performed using the Nonlinear Analysis of Geotechnical (ANLOG)

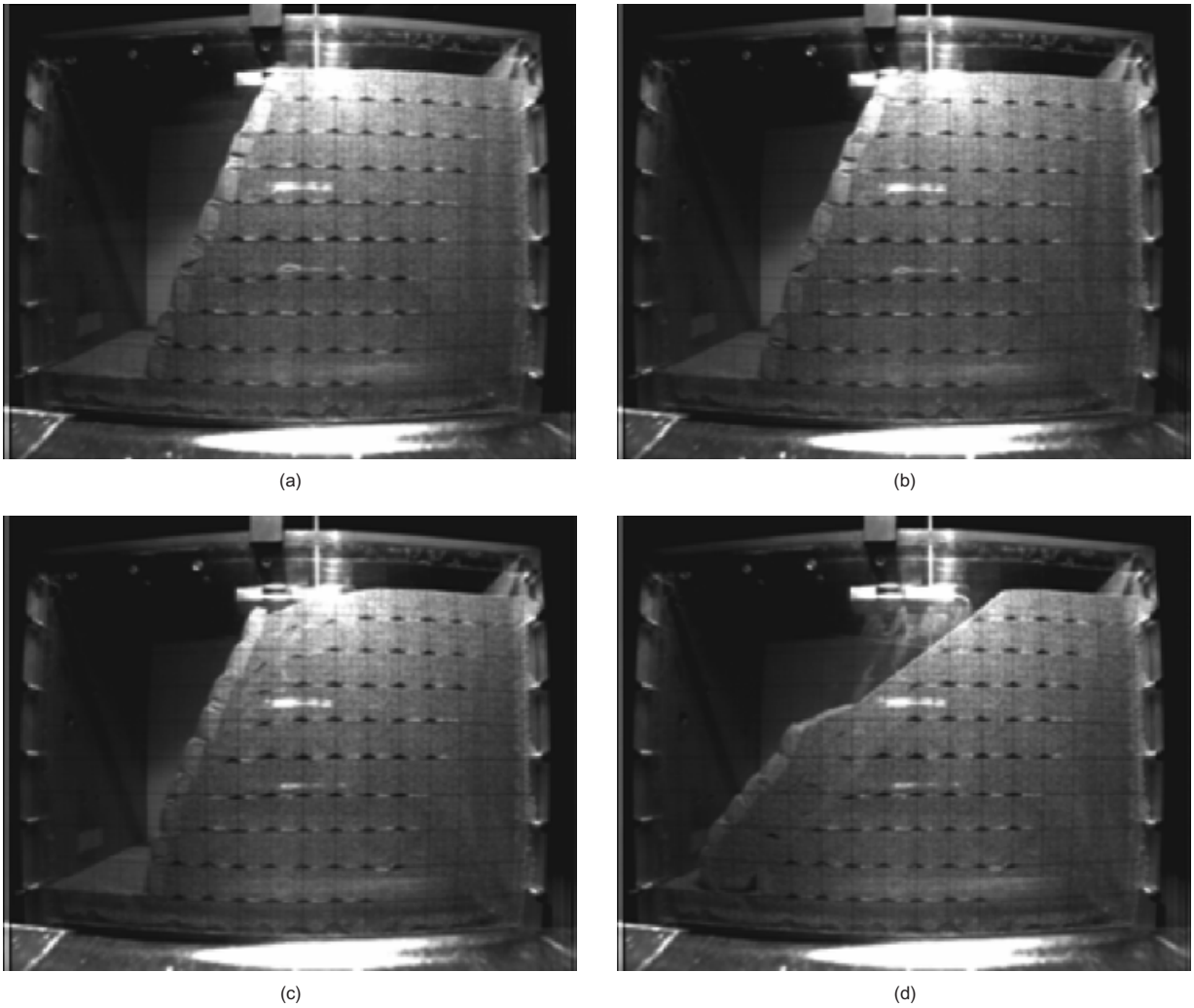

Figure 2. Photographs of centrifuge slope model M1: (a) initial condition (1*g*); (b) working stress (10*g*, FS = 2.0); (c) progressive failure (40*g*, FS = 1.1); (d) failure (50g, FS = 1.0)

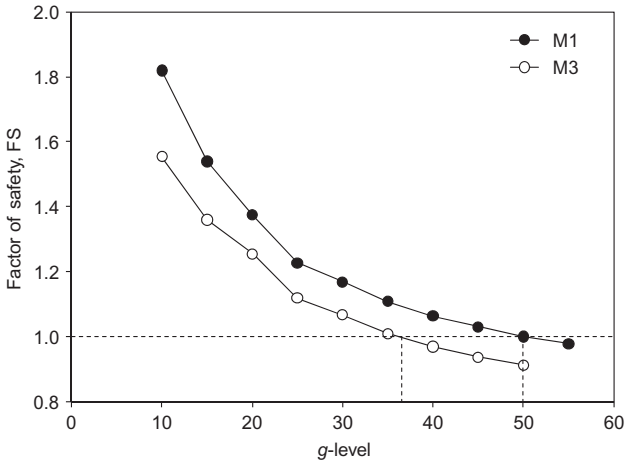

Figure 3. Calculated factor of safety against *g*-level for Models M1 and M3

program, an in-house program coded in Fortran. Initial settings of the finite element model, advanced soil and reinforcement models and integration algorithm are also discussed below.

3.1. Initial settings

Figure 1b shows the initial settings of a finite element model for centrifuge Models M1 and M3. An eight-node quadratic quadrilateral element under plane-strain conditions was designated for the solid element. Reinforcements were simulated using a three-node quadratic truss with only one degree of freedom in the horizontal direction. The numerical model also included secondary reinforcements to simulate the overlap layer (50 mm long) in the centrifuge model. Standard boundaries were imposed to simulate confinement to the edges of the aluminium centrifuge box. Stages were constructed layer by layer. Mesh updating was used to model large deformations.

The centrifugal force of the centrifuge was simulated by increasing the body force on each element. In each loading stage, the simulation increased the load by 5*g*. Notably, the calculated FE failure was earlier than the actual failure observed in the test. The finite element simulations terminated at the next loading increment after completing 45*g* for Model M1 and 30*g* for Model M3, owing to numerical difficulties in the computation.

3.2. Backfill model and properties

To model soil behaviour in various stress states, the Lade and Kim soil constitutive model (Kim and Lade 1988; Lade and Kim 1988a, 1988b, 1995; Lade and Jakobsen 2002) combined with a modified softening model (Yang 2009) was implemented in the ANLOG program. The Lade–Kim soil constitutive model, which is an elasto-plastic model, includes the following components: elastic model, failure criterion, plastic potential function for non-associated flow rule, yield criterion, isotropic hardening and softening laws. See Lade and Jakobsen (2002) for details.

Among all the components of the Lade–Kim soil model, the softening laws govern the soil softening behaviour numerically by yield surface contraction. As the soil strength changes from hardening (pre-peak) to softening (post-peak), the yield surface changes from expansion to contraction, as illustrated in Figure 4. The original softening model proposed by Lade and Kim is an exponential decay function of plastic work W_p, given by

$$f''_p = A\mathrm{e}^{-BW_p/p_a} \tag{1}$$

in which f''_p is the size of the yield surface; W_p is the plastic work; p_a is atmospheric pressure; and A and B are positive constants that can be determined using the hardening curve at stress level $S = 1$, which is the stress level at the peak shear strength of the soil.

The major problem in the original softening model is that the size of the yield surface can mathematically contract to zero if plastic work is high. However, in reality, the stress state should remain at a residual strength when the soil experiences large deformation. Further, numerical instability may occur if the decrease in yield surface is not limited during softening. The proposed solution is a modified softening model that uses an inverse sigmoid function. Figure 4 shows the concept of the modified softening model in f''_p and W_p space. The figure shows how the modified softening law can limit the decrease in yield surface size at a residual yield surface f''_{pr}, the minimum size of yield surface during softening. The governing equation for the modified soil softening model is

$$f''_p = \left(f''_p\right)_{S=1} - \frac{1}{c + a\exp\{-b[(W_p/p_a) - (W_p/p_a)_{S=1}]\}} \tag{2}$$

where $(f''_p)_{S=1}$ is the size of the yield surface at $S = 1$, and $(W_p/p_a)_{S=1}$ is the value of the normalised plastic work at $S = 1$. Both $(f''_p)_{S=1}$ and $(W_p/p_a)_{S=1}$ can be evaluated using the Lade–Kim soil model from the hardening curve at $S = 1$. The equation for calculating c is

$$c = \frac{1}{\left(f''_p\right)_{S=1} - f''_{pr}} \tag{3}$$

where f''_{pr} is the yield function in the residual condition, as addressed previously. The value of f''_{pr} can be obtained by substituting the stress components in the residual stress state into the yield criterion $f'_p(\sigma)$ using equation 13 in Lade and Jakobsen (2002). The three material parameters are a, b and f''_{pr}, which are positive, dimensionless real numbers. The parameters for the model were calibrated from a set of triaxial compression tests using Monterey No. 30 sand. In this case, softening parameters *a, b* and f''_{pr} correlate with confining pressures, and can be regressed as linear functions of confining pressures.

Figure 5 shows the predicted stress–strain responses of Monterey No. 30 sand for $D_r = 70\%$ and 50%, and compares them with those obtained in triaxial compression tests. Figure 5 shows that applying the modified softening model in the Lade-Kim soil model accurately captures stress–strain relations, particularly in the soil post-peak region. Table 2 summarises the calibrated parameter values for Monterey No. 30 sand. Finally, soil with low cohesion (1 kPa) was applied to the backfill elements along the slope face, not only to simulate the confinement of soil to the wrap-around facing, but also to improve the numerical stability, particularly where the confinement was low. Soil with a cohesion of 10 kPa was applied to the foundation elements to simulate the effect of a denser foundation, as in the centrifuge models. The cohesion in the Lade–Kim model is computed as $a'p_a$, where a' is one of the failure criterion parameters, and p_a is atmospheric pressure. Thus a' was set to 0.01 for the backfill along the slope face and to 0.1 for the foundation.

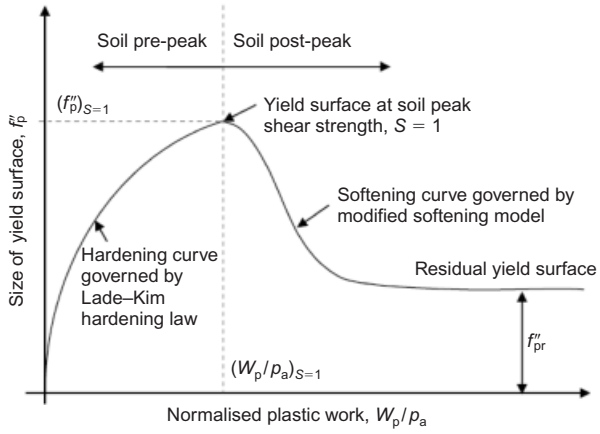

Figure 4. Illustration of Lade–Kim hardening laws and modified softening model

3.3. Reinforcement model and properties

A non-linear elastic reinforcement model based on a second-order polynomial was used to equate tensile load to tensile strain (Karpurapu and Bathurst 1995). The governing equation and incremental form are

$$T(\varepsilon) = C_1\varepsilon + C_2\varepsilon^2 \tag{4}$$

$$\frac{\mathrm{d}T(\varepsilon)}{\mathrm{d}\varepsilon} = C_1 + 2C_2\varepsilon \tag{5}$$

where T is the reinforcement tensile load, and ε is the corresponding tensile strain. The parameters C_1 and C_2

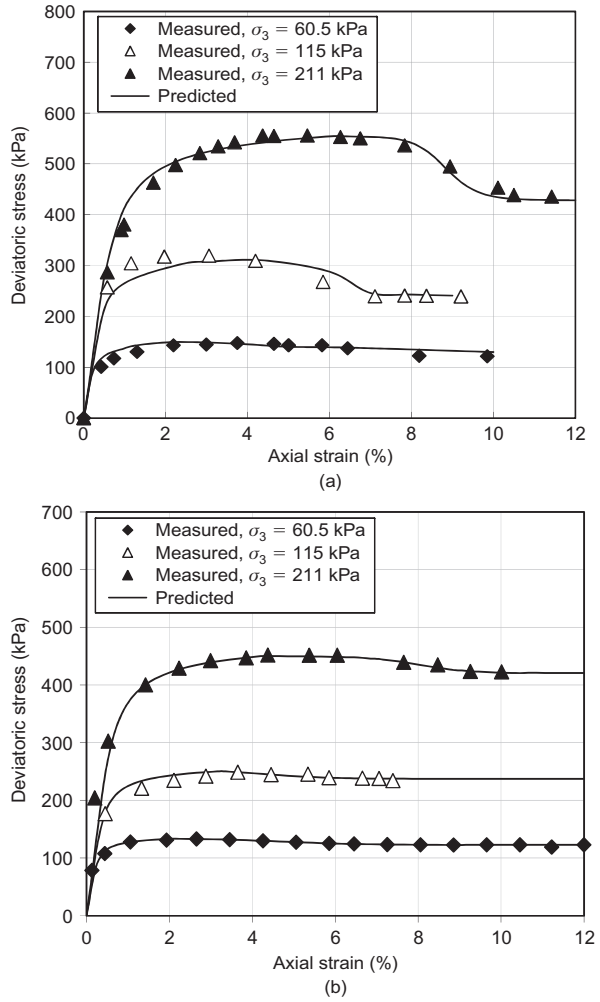

Figure 5. Comparison of predicted and measured stress–strain response of Monterey No. 30 sand: (a) $D_r = 70\%$; (b) $D_r = 50\%$

are the initial stiffness and strain-softening coefficient, respectively. Equation 5 is the implementation formula, which also indicates the reinforcement tangential stiffness.

When simulating reinforcement behaviour within centrifuge models, the confined load–strain response should be used to model the nonwoven geotextile, as discussed previously. Soil confinement reportedly affects the load–strain response of the nonwoven geotextile by increasing reinforcement tensile strength and stiffness. However, the strain levels are not significantly affected by soil confinement (e.g. Leshchinsky and Field 1987; Wu 1991; Ling *et al.* 1992; Ballegeer and Wu 1993). Specifically, the strain at failure remains at approximately the same value at all confinement levels. As a result, the load–strain response of a nonwoven geotextile under soil confinement in this study is assumed to exhibit a trend similar to that observed in wide-width tensile tests under unconfined conditions, except that the unconfined curve is multiplied by the ratio of the ultimate confined tensile strength to the ultimate unconfined tensile strength: that is

$$T_{\text{confined}} = T_{\text{unconfined}} \times \frac{T_{\text{ult\_confined}}}{T_{\text{ult\_unconfined}}} \tag{6}$$

where T_{confined} is the mobilised confined tensile load at any reinforcement strain of interest; $T_{\text{unconfined}}$ is the mobilised unconfined tensile load associated with the reinforcement strain; and $T_{\text{ult\_unconfined}}$ is the ultimate unconfined tensile strength. The values of $T_{\text{unconfined}}$ and $T_{\text{ult\_unconfined}}$ can be obtained from the conventional wide-width tensile test, as shown in Figure 6. The $T_{ult\_confined}$ is the ultimate confined tensile strength of geotextile back-calculated in the limit equilibrium analysis discussed previously. Figure 6 shows the confined load strain response of the nonwoven geotextile estimated using Equation 6. Last, the reinforcement model parameters are calibrated to the confined load–strain response of the reinforcement in order to obtain the reinforcement parameters $C_1 = 1.4$ and $C_2 = -4.85$. Figure 6 also shows the calibration results.

3.4. Soil–reinforcement interaction

In ANLOG, the interaction and relative movement between the reinforcement layer and backfill can be modelled as linear spring-slider systems with interface shear strength defined by the Mohr–Coulomb failure criterion. A sensitivity study was performed to test the effectiveness

Table 2. Summary of material properties for Lake-Kim model and modified softening model

Model component	Parameter	D_r	
		70%	50%
Unit weight	γ (kN/m^3)	16.0	15.7
Elastic model	M, λ, ν	705, 0.257, 0.35	705, 0.257, 0.35
Failure criterion	m, η_1, a'	0.0214, 29.3, 0	0.0214, 20.4, 0
Plastic potential	ψ_2, μ	−8.51, 2.2	-8.51, 2.4
Yield criterion	h, α	0.67, 0.2	0.67, 0.2
Hardening model	C, p	5.07×10^{-5}, 1.9	5.07×10^{-5}, 1.9
Modified softening model	(expressed by a linear function of confining pressures)		
	a	$a = 0.0076\sigma_3 + 0.27$	$a = -0.0039\sigma_3 + 2.54$
	b	$b = -0.737\sigma_3 + 209.8$	b $= -0.316\sigma_3 + 102.0$
	f''_{pr}	$f''_{pr} = 0.30\sigma_3 + 20.9$	$f''_{pr} = 0.38\sigma_3 + 30.9$

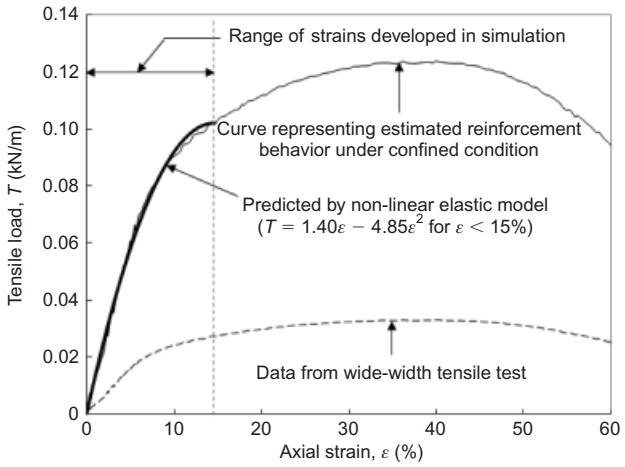

Figure 6. Unconfined and confined reinforcement tensile strengths and prediction results

of the interface elements for predicting slope response. The sensitivity test results showed that the interface element has a negligible effect on the computation results (i.e. the calculated relative displacement between soil and reinforcement is less than 0.1 mm). However, simulating the soil–reinforcement interface substantially increases the computational cost and the chances of numerical instability. Therefore the finite element analysis in this study excluded interface elements.

Since this approach does not consider relative displacement between soil and reinforcement in numerical mode, pullout of the reinforcement from the backfill is not simulated. Use of this numerical modelling approach was supported by visual inspection after slope collapse. The failure of the slope resulted from breakage of the reinforcement rather than pullout. Last, this approach was also supported by other finite element simulations of reinforced-soil segmental walls under both working stress and surcharge load conditions. For example, the simulation results obtained by Hatami and Bathurst (2005, 2006) were consistent with measured wall responses, even without adoption of the soil–reinforcement interface element in their FE models.

3.5. Computational algorithm

The forward Euler scheme is a typical scheme for integrating stress in a conventional FE program. However, this scheme turns out to be computationally expensive and inefficient, because it is incapable of using different sizes of strain subdivision for different soil stress states. Additionally, the scheme cannot determine the accuracy of stress integration. Jakobsen and Lade (2002) found that, compared with the original forward Euler scheme, the modified forward Euler scheme achieved superior computational accuracy and efficiency. The stress integration scheme also improves convergence and computational accuracy in global iteration processes, which depend on the applied stress–strain relation. Therefore this study implemented the modified forward Euler scheme with error control, in which the size of each strain subincrement is determined so that the absolutely necessary number of strain subdivisions is used to fulfil the specified tolerance, which was set as 10^{-3}. For convergence in the global iteration process, a Newton–Raphson iterative scheme was adopted, and the global convergence criteria (i.e. unbalanced force divided by current external force) was selected, based on a series of parametric analyses performed to optimise accuracy and computation speed concurrently.

4. MODEL VERIFICATION

4.1. Deformation pattern

The simulation results were compared with the centrifuge results to verify the accuracy of the proposed FE model. Figure 7 qualitatively compares the slope deformation patterns in Model M1. Model M3, which has a similar deformation pattern, is not shown. Figure 7a shows the centrifuge model M1 at the moment of failure at 50*g*. Figure 7b shows the deformed meshes (20× enlargement for better visualisation), total displacement contours and vectors of the FE model at 45*g*. Overall, the FE model satisfactorily captures the deformation pattern of the centrifuge model. For a more detailed comparison, deformations were also analysed at the sliding slope mass, at the rear of the slope crest, and at the slope face at the second reinforcement layer. First, the sliding slope mass showed similar trends in both centrifugal and numerical models. Second, the settlement at the rear of the slope crest revealed by the centrifuge model was also observable in the numerical model by comparing the original and deformed meshes at the rear of the slope crest, as

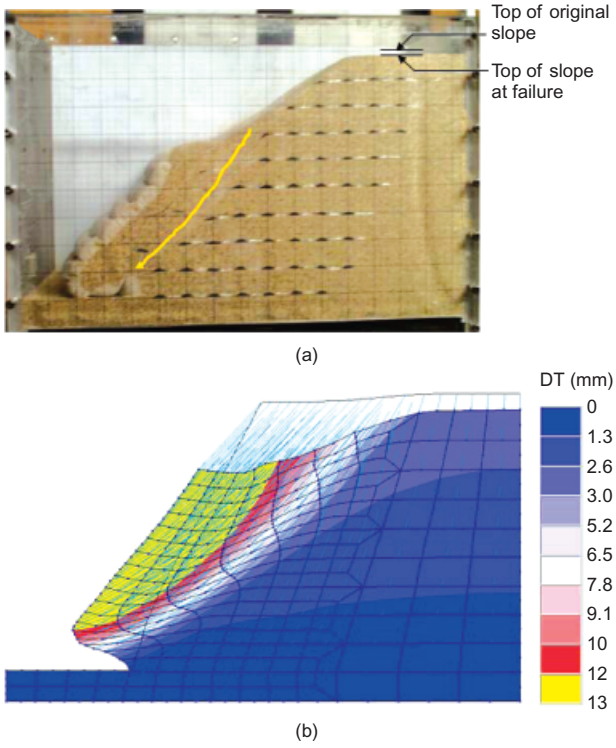

Figure 7. Comparison of deformation pattern of Model M1: (a) centrifuge model at 50*g*; (b) FE model at 45*g* (deformation mesh × 20)

indicated in Figure 7b. Third, the failure surface in Model M1 passed through the slope face at the second reinforcement layer rather than at the slope toe, as assumed in conventional limit equilibrium analyses. Figure 7b shows that the FE simulation captures similar behaviour. The next section discusses possible reasons why the failure surface did not pass through the slope toe.

4.2. Location of failure surface

Figures 8 and 9 show the locations of the measured and predicted failure surfaces in the two slope models. The failure surface of the centrifuge slope model was identified by the tears (ruptures) observed in each reinforcement layer. The tears are indicated by the blue triangles in

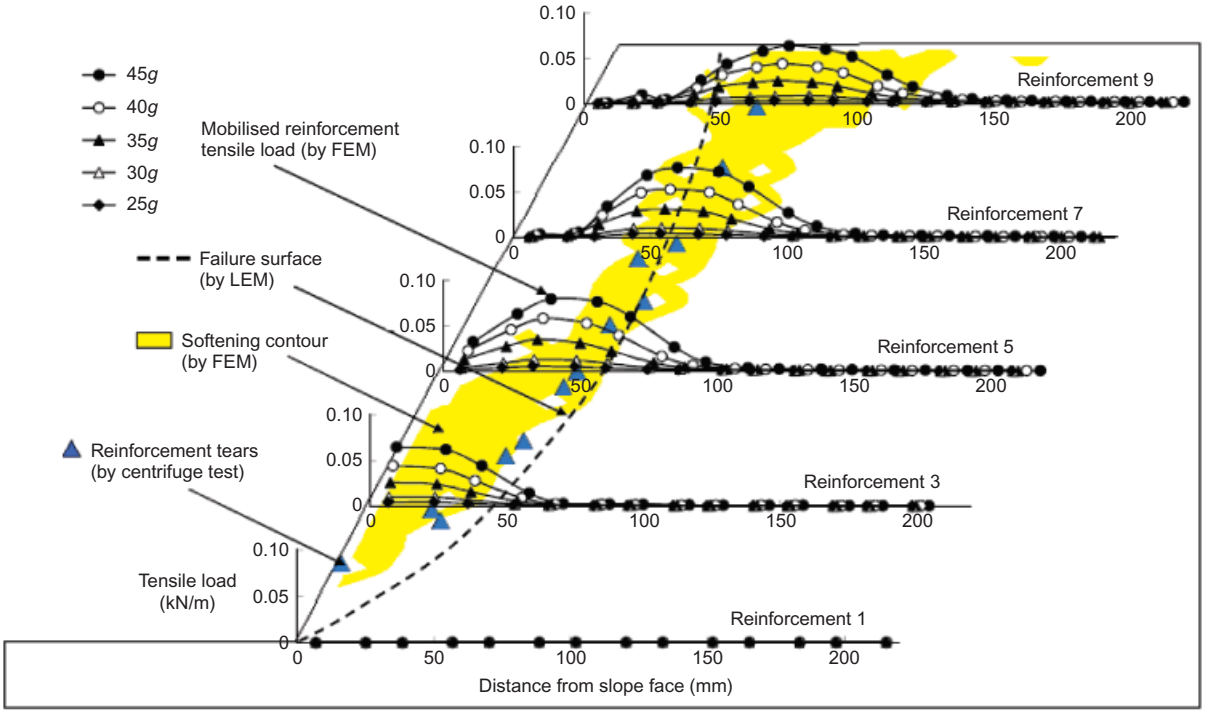

Figure 8. Comparison of failure surface locations in Model M1

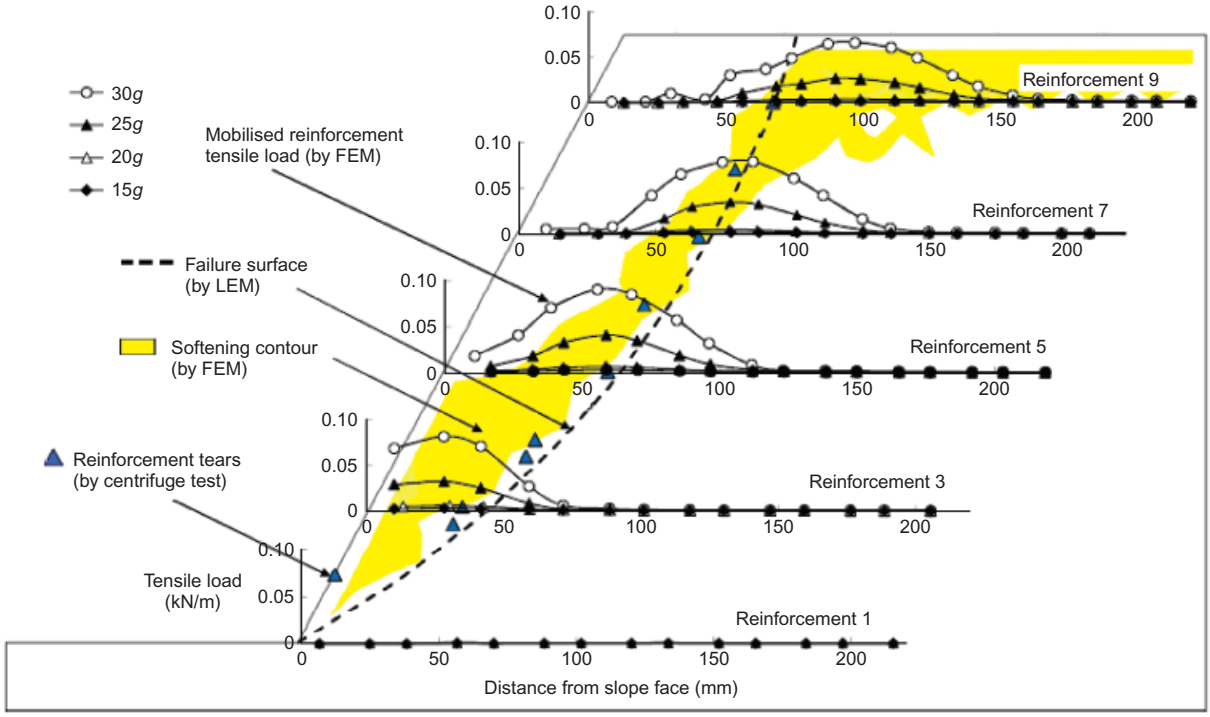

Figure 9. Comparison of failure surface locations in Model M3

Figures 8 and 9. The failure surface in limit equilibrium analysis was identified by searching for the critical slip surface. The failure surface in the FE model was defined as the contour of soil softening. The FE and centrifuge models showed good agreement in failure surface location. Both showed that the failure surface passed through the slope face in the second reinforcement layer, rather than at the slope toe. Because the failure surface in the limit equilibrium analysis passed through the slope toe, the predicted failure surface differs slightly from those identified by the other analyses.

The boundary constraint from the denser and shallower foundation in the centrifuge models probably prevented the surfaces from passing through the slope toe. This denser foundation constrained the soil movement as well as reinforcement deformation at the base of slope. Therefore strains that develop in the first (lowermost) reinforcement layer are too small to cause failure. For example, Figures 8 and 9 show that the tensile loads that developed at the first reinforcement layer were negligible at all *g*-levels. This observation confirms the observations by Zornberg *et al.* (1998a) in their analyses of retrieved reinforcements from centrifuge models, in which the lowermost geotextile layer consistently showed no evidence of tears or severe strain. Allen *et al.* (2003) addressed similar attenuating effects of stiff competent foundations on reinforcement loads at the base of the wall.

Figures 8 and 9 also show that the failure surface corresponds to the locus of the maximum reinforcement tension at each layer. This correlation is consistent with the field observations of a full-scale, instrumented reinforced soil slope in Zornberg (1994), which showed that the maximum strain in each instrumented reinforcement layer corresponds to the trace of potential failure surface in the slope.

4.3. Slope settlement

Figure 10 compares the settlement at the front crest of the slopes obtained in Models M1 and M3 with the actual settlement measured by LVDT. In the centrifuge test, the slope model started in the vertical position and then changed to the horizontal position after the centrifuge started to spin. At the first loading increment, this change in position probably introduced further deformation that could not be simulated in the FE model. Therefore the data obtained from the first *g*-level increment are excluded from the comparison. Both measured and predicted settlement are offset to the condition at 5*g*. In general, the comparison shows good agreement except for the last loading increment, in which FE underestimates the measured data.

5. RESULTS AND DISCUSSION

After verifying the FE model, soil stress data and reinforcement tensile load data can be obtained. This section discusses the observed distribution and development of soil stresses and reinforcement tensile loads, and the resulting insights into GRS structure design.

5.1. Soil stress information

Soil stress mobilisation can be described by the soil stress level S, which is defined as the ratio of the current failure envelope f_n (associated with the mobilised soil shear strength) to the failure criterion η_1 (associated with the peak soil shear strength). Figure 11 illustrates typical soil stress level contours within a slope, and the corresponding stress states. The value of S is less than 1.0 when the current stress state is far away from peak shear strength (Figure 11a).

$$S = \frac{f_n}{\eta_1} \text{ (for } S < 1) \tag{7}$$

The value of S equals 1.0 when the current soil stress state reaches its peak shear strength (Figure 11b).

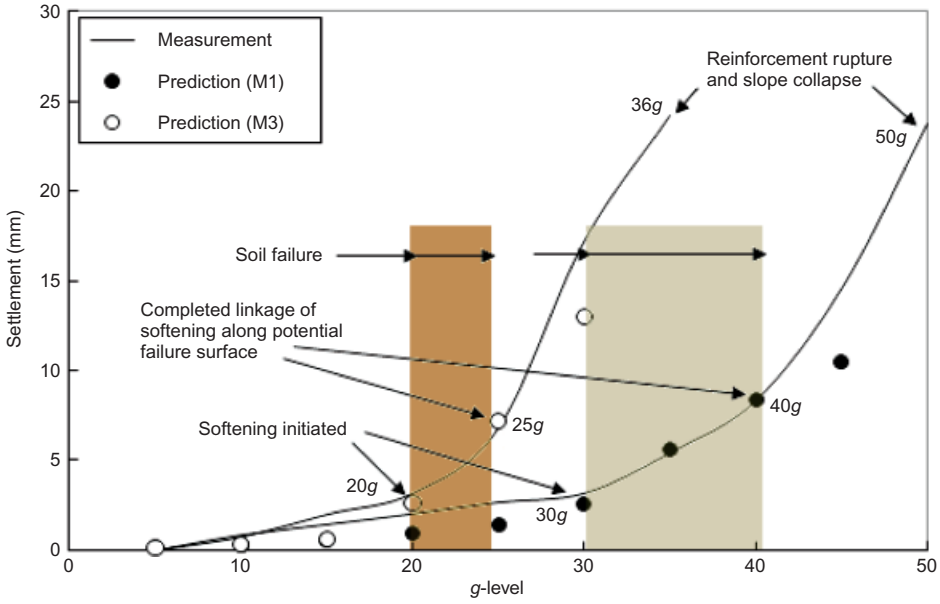

Figure 10. Comparison of settlement with *g*-level for Models M1 and M3

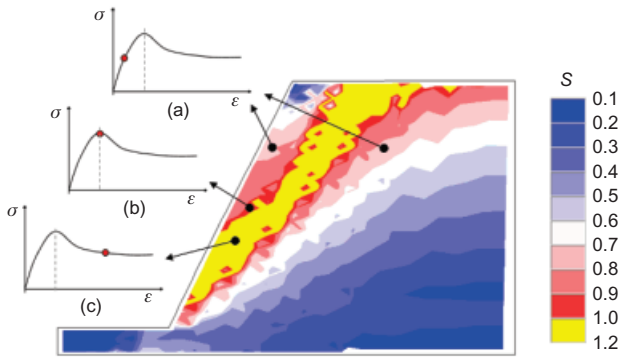

Figure 11. Soil stress level contour and corresponding stress states: (a) $S < 1$; (b) $S = 1$; (c) $S > 1$

$$S = \frac{f_n = \eta_1}{\eta_1} \text{ (for } S = 1) \tag{8}$$

The value of S is assigned to be larger than 1.0 when the soil stress state crosses the peak shear strength and reaches the soil post-peak region (Figure 11c).

$$S = 1 + \left(1 - \frac{f_n}{\eta_1}\right) \text{ (for } S > 1) \tag{9}$$

In the soil post-peak region, S ranges from 1.0 to 2.0. When $S = 2$, the current failure envelope f_n returns to zero. $S = 2$ is an upper-bound value, ideally; in fact, S is always less than 2 because the soil stresses during softening are limited to soil in a residual state, and do not decrease to zero.

Figures 12 and 13 show the values for S obtained for varying g-levels in Models M1 and M3, respectively. In both models, the backfill stress that develops with increased load propagates along the potential failure surface. Two high stress level areas reach 0.9 at the top and toe of the slopes (Figures 12a and 13a). Immediately after the stress level reaches peak ($S = 1$), strength softening occurs at the top and toe of the slope at approximately 30g (FS = 1.16) in Model M1, and at approximately 20g (FS = 1.25) in Model M3 (Figures 12b and 13b, respectively). The softening occurs randomly and irregularly along the failure surface (Figures 12c and 13c), and then forms a clear softening band (Figures 12d and 13d). The completed linkage of the soil-softening band throughout the entire potential failure surface occurs at approximately 40g (FS = 1.06) in Model M1, and at approximately 25g (FS = 1.1) in Model M3 (Figures 12e and 13e, respectively).

The observed formation of failure surfaces observed in this study is consistent with several studies of the shear behaviour of sand in the context of shear band development (e.g. Yoshida *et al.* 1993; Yoshida and Tatsuoka 1997; Suzuki and Yamada 2006). For instance, Suzuki and Yamada (2006) described the typical progressive failure of sand in the drained triaxial test. They observed that, as loading increases, tiny dilative strain areas occur 'randomly' at various locations. The dilative strain areas indicate the places where soil softening is likely to occur. When the loading approaches soil peak strength, a shear band forms from areas of dilative strain.

The observed results for S have two design implications. First, Figures 12 and 13 show that the mobilisation of S is clearly non-uniform along the failure surface. This observation contradicts current assumptions regarding the internal stability of GRS structures. That is, current design methods based on earth pressure theory or the limit equilibrium method assume that the soil shear strength along the failure surface mobilises equally, and reaches peak shear strength simultaneously. Second, the current design requires FS $\geqslant$ 1.3 to achieve global stability in a reinforced slope. In contrast, Figures 12 and 13 show that, in both slope models, soil softening has not initiated at FS $\geqslant$ 1.3. Therefore the soil stress state is still below its peak shear strength at FS $\geqslant$ 1.3. This suggests that FS $\geqslant$ 1.3 is a good criterion for ensuring the serviceability of slopes (i.e. the developed soil stress state is under work stress conditions).

5.2. Soil strain information

Analysis of the soil strain data obtained from the numerical simulation showed that the failure surface corresponds to the locus of intense soil strains in the horizontal, vertical and shear directions (Figure 14). This clearly indicates significant deformation along the failure surface. Because of the dilatancy of frictional materials, the soil horizontal strain along the failure surface is apparently under tension, according to the negative value of strain indicated in Figure 14a. Apparently, the final slope failure (sliding of the active reinforced wedge) results from large displacements along the failure surface. When the deformation-induced soil strains reach a certain intensity, the mobilised reinforcement tensile loads reach their peak values (reinforcement breakage occurs) and cause the final failure of slope.

5.3. Soil stress state and slope settlement

An important point obtained from the simulation is the relationship between soil stress state and slope deformation. Figure 10 shows that slope deformation correlates with soil stress state. The FE results indicate that the inflection point in settlement (increase in settlement rate) corresponds to the status of soil softening along the failure surface in both models. The first point of inflection indicates the initiation of soil softening (at 30g and 20g for Models M1 and M3, respectively), and the second point indicates the completed linkage of softening along the failure surface (at 40g and 25g for Models M1 and M3, respectively). Between these two points of inflection, the slopes of the settlement curve can be divided into three approximately linear sections corresponding to the periods before, during and after soil softening developed along the failure surface. Similar observations were reported by Bathurst (1993) and Karpurapu and Bathurst (1995) in tests of two instrumented, large-scale GRS retaining walls in the Royal Military College retaining-wall test facility. They reported that the rate of facial displacement increased significantly at soil failure. Differently from this study, the soil failure observed in their tests was defined as the development of a well-developed shear plane.

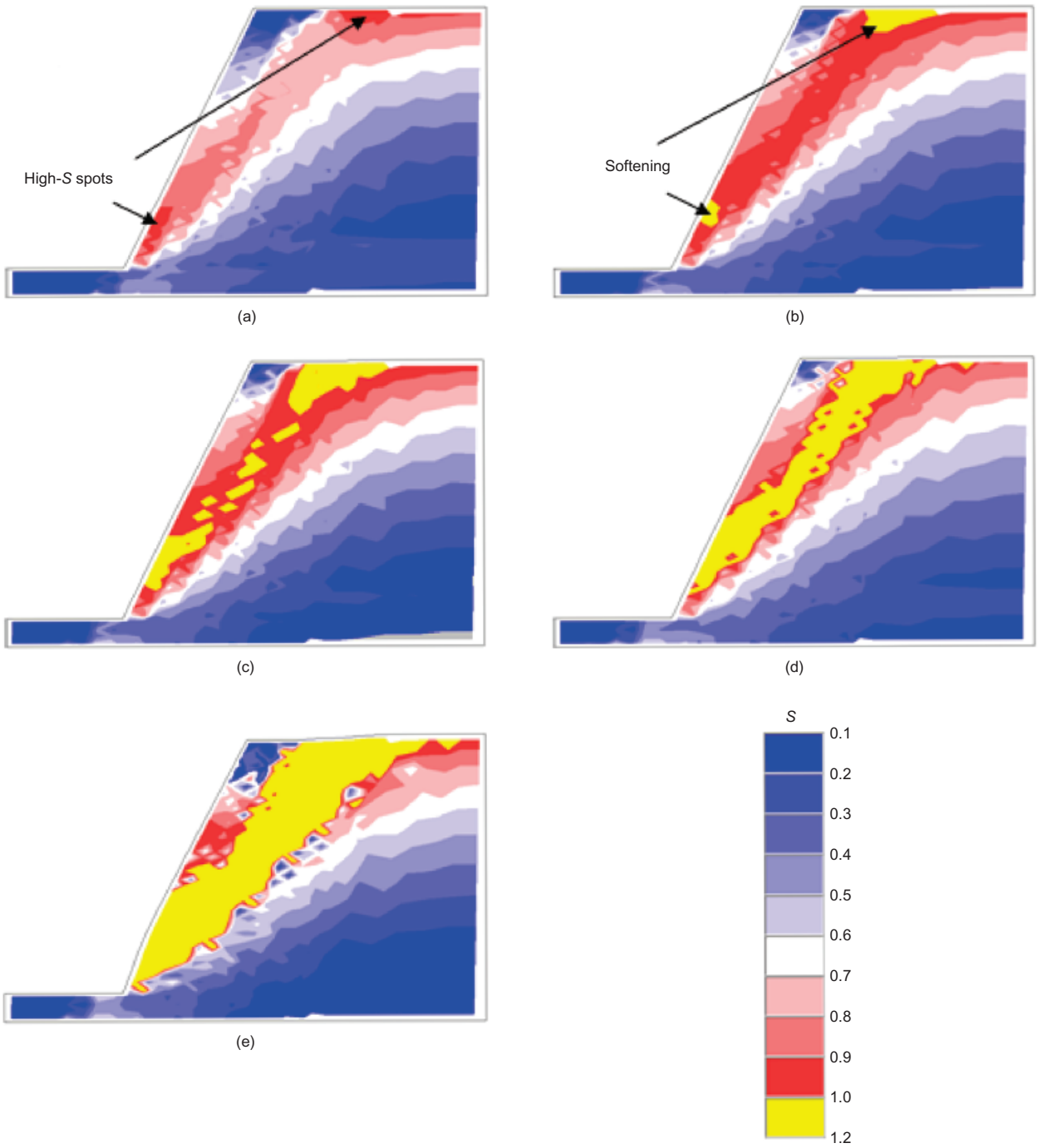

Figure 12. Stress level distribution and development for Model M1: (a) 20*g*, FS = 1.37; (b) 30*g*, FS = 1.16; (c) 32*g*, FS = 1.13; (d) 35*g*, FS = 1.10; (e) 40*g*, FS = 1.06

5.4. Effect of soil shear strength on slope stability

The selection of shear strength properties (peak against residual shear strength) for the design of GRS retaining structures has been a question under debate (Leshchinsky 2001; Zornberg and Leshchinsky 2001; Zornberg 2002a, 2002b, 2002c, 2002d, 2003). Zornberg *et al.* (1998a), in a comparison of the failure *g*-levels of two centrifuge models with different densities, found that the slope models with higher backfill density failed at higher *g*-levels compared with models with lower backfill densities but similar reinforcement spacing and type. Since backfill with different densities affects only peak shear strength, and maintains the same residual shear strength, the higher *g*-level at failure in the denser models is clearly attributable to the higher peak soil shear strength in these models. The authors therefore concluded that the peak strength, not the residual strength, of the soil governs the stability of GRS structures, and further recommended that using peak shear strength parameters when designing GRS structures should be standard practice in the USA.

The stress information obtained from the simulation is used to explain the observed difference of failure *g*-level due to different soil densities, and to understand the soil strength properties governing structural stability. As in

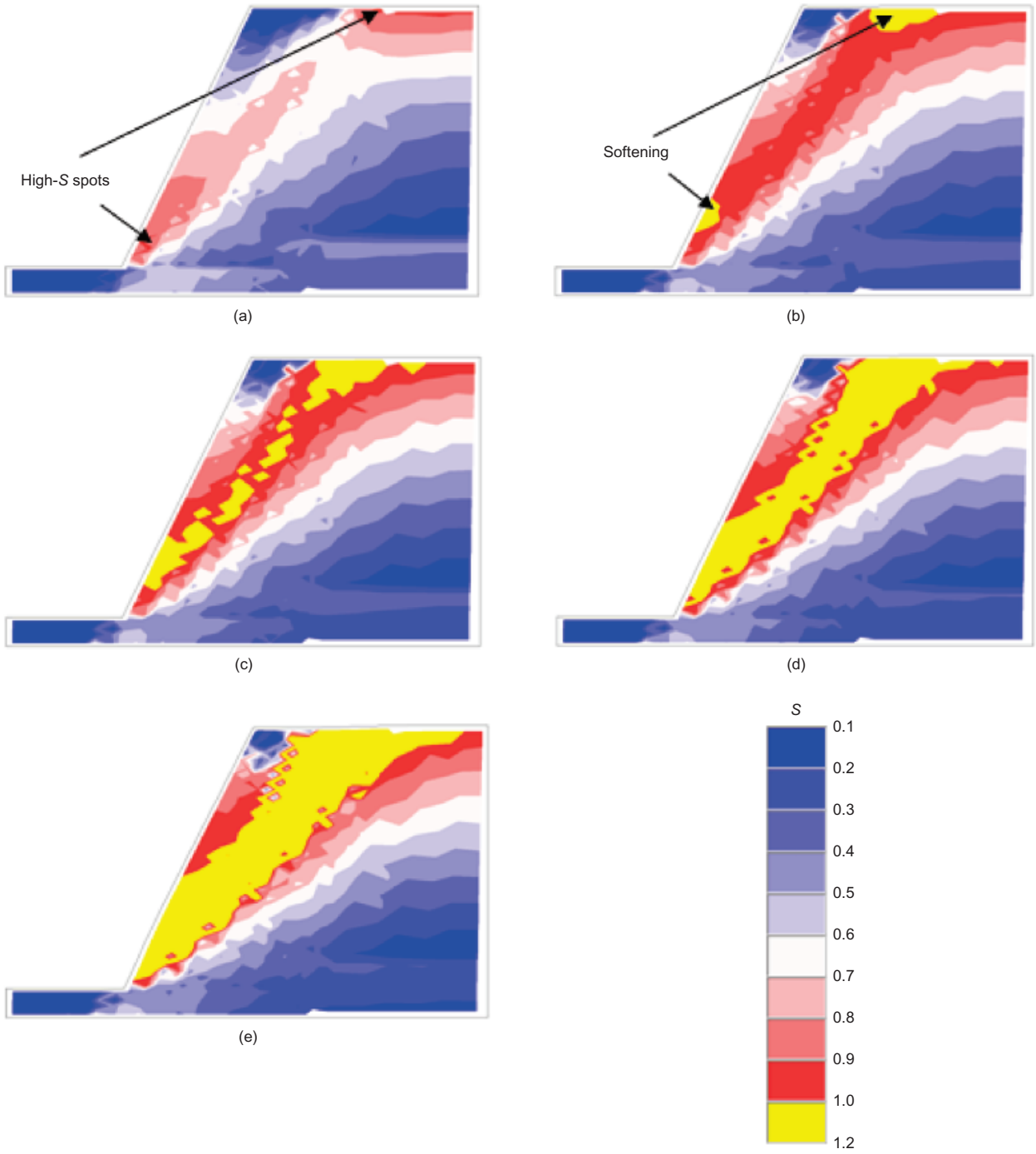

Figure 13. Stress level distribution and development for Model M3: (a) 15*g*, FS = 1.36; (b) 20*g*, FS = 1.25; (c) 21*g*, FS = 1.22; (d) 23*g*, FS = 1.16; (e) 25*g*, FS = 1.1

Zornberg *et al.* (1998a), the numerical results show that soil softening and slope failure occur earlier (at lower *g*-levels) in Model M3 than in Model M1. The duration of soil softening (the *g*-level increment from the initiation of soil softening to the completed linkage of soil softening) is also shorter in Model M3 than in Model M1 (Figure 10). The explanations for these numerical observations are as follows.

The simulation models the effect of different soil peak shear strengths for different soil densities by using different input values of the failure criterion parameter η_1. (see Table 2). One can envisage that the failure criterion parameter η_1 in the Lade–Kim model is analogous to the friction angle ϕ in the Mohr–Coulomb model. Figure 15 illustrates that failure criteria parameter η_1 in the octahedral plane represents the size of the peak failure envelope of the soil. Because of the lower soil density, η_1 has a lower value in Model M3 than in Model M1 (20.4 compared with 29.3, respectively). Accordingly, the size of the peak failure envelope in Model M3 is smaller than that in Model M1 (Figure 15). Before applying centrifugal force, the developed soil stresses in both models are negligible, and should be close to the origin of the octahedral plane. As the *g*-level incrementally increases,

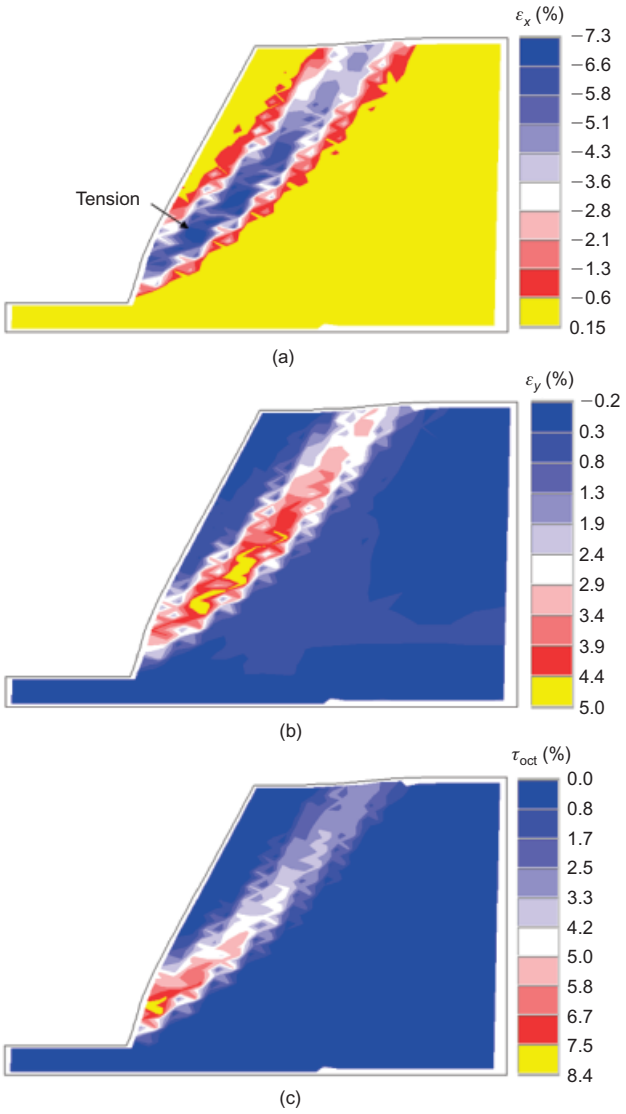

Figure 14. Soil strain distribution at 45*g* for Model M1: (a) horizontal strain, ε_x; (b) vertical strain, ε_y; (c) shear strain in octahedral plane, τ_{oct}

the development of soil stresses follows a similar loading path in the two slope models. The loading path reaches the peak failure envelope earlier in Model M3 (smaller failure envelope) than in Model M1 (larger failure envelope). When the soil stresses reach the peak failure envelope of Model M3, soil softening is initiated immediately. That is, soil softening is initiated earlier in Model M3. Finally, because the two slope models have the same soil residual strength and reinforcement tensile strength, slope failure also occurs earlier in Model M3. In summary, the numerical results show that the soil stress state must first cross the *threshold* of soil peak shear strength before soil softening and slope failure occur: therefore numerical simulations show that peak shear strength, not residual shear strength, governs system stability.

5.5. Reinforcement tensile load

The reinforcement tensile load data obtained in the simulations are used to study the mobilisation and distribution of reinforcement tensile loads in various soil stress states. Figure 16 show the distribution and development of maximum tensile load in each reinforcement layer for various *g*-levels in Models M1 and M3. Two important observations are noted. First, the mobilisation of reinforcement tensile load does not correlate with the load. Mobilisation of the tensile load in each reinforcement layer is insignificant before soil softening occurs. Afterward, however, mobilisation of the reinforcement tensile load becomes significant: roughly 20% in Model M1 and 40% in Model M3 with each 5*g* increment. The mobilisation of reinforcement tensile loads at the initiation of soil softening is highlighted in red in Figure 16. The lack of significant mobilisation of reinforcement tensile loads before soil softening occurs contradicts the current design methods for evaluating the maximum reinforcement tensile load T_{max} at each reinforcement layer. Such methods assume that the reinforcement tensile load is significantly mobilised to resist the lateral active earth forces, assuming full mobilisation of soil peak shear strength.

The significant mobilisation of reinforcement tensile load after soil softening indicates load transfer from soil to reinforcement. At the soil post-peak stage, the reinforcement tensile loads have to be mobilised significantly in order to offset the increasing centrifuge loading and, concurrently, the decreasing soil strength (dropping from peak to residual strength). Although the mobilisation of reinforcement tensile loads at the soil post-peak stage maintains system stability, the incremental system deformation increases rapidly (Figure 10). Depending on the tensile strength of the reinforcement, system failure (FS = 1.0) may occur after only a few loading increments.

A second observation in Figure 16 is the distribution of maximum reinforcement tensile loads with depth for various loading increments. Figure 16 shows a nearly uniform distribution of maximum reinforcement tensile loads with depth at low *g*-levels before soil softening begins. This distribution agrees with the field measurements obtained for instrumented GRS walls under working stress conditions (Allen *et al.* 2003; Bathurst *et al.* 2008). The distribution of maximum reinforcement tensile loads at high *g*-levels (after soil softening occurs) depicts a trapezoidal shape, with the location of the peak value at the mid-height of the reinforced slopes. This observation generally agrees with the failure conditions observed in other experimental centrifuge tests of GRS slopes. For example, in the centrifuge models in Zornberg *et al.* (1998a) and Zornberg and Arriaga (2003), the analyses of reinforcement strains showed that the peak reinforcement strain developed at locations consistent with those observed in this study.

The observed distribution of reinforcement tensile loads in the simulations does not support the triangular distribution with depth (proportional to the overburden pressure) assumed in current design methodologies for geosynthetic structures (Figure 17a). This finding has major design implications because the current definition of reinforcement layout assumes that the most critical zone is at the base of the structure. Figures 17b and 17c propose alternative distributions of maximum reinforcement tensile loads with depth for both working stress and large soil strain conditions, respectively.

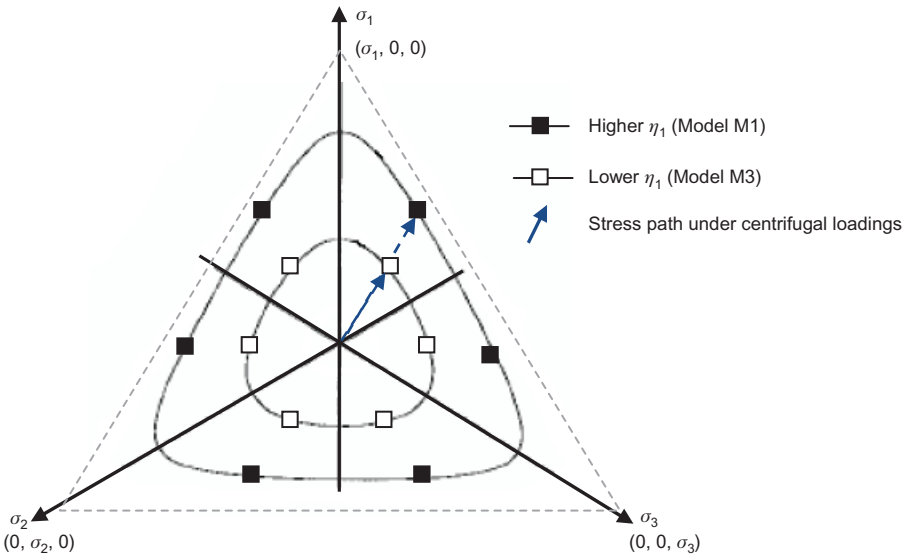

Figure 15. Illustration of failure envelope and stress path in the octahedral plane

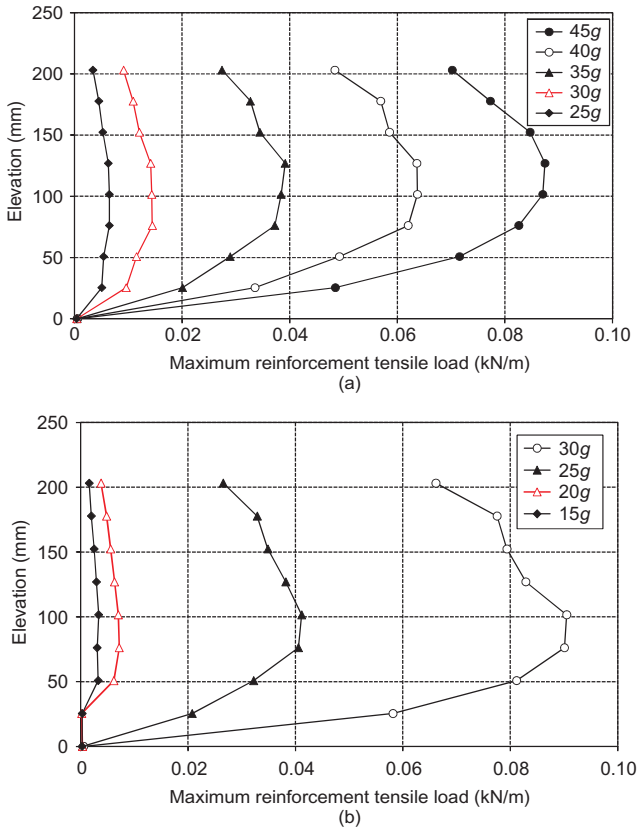

Figure 16. Distribution and development of maximum reinforcement tensile load with depth at each reinforcement layer: (a) Model M1; (b) Model M3

5.6. Comparison of FS by finite element and limit equilibrium methods

Although different definitions of FS have been applied in the limit equilibrium method, the generic definition of FS in the limit equilibrium method, relative to the shear strength of the soil, is the available soil shear strength divided by the mobilised soil shear stress needed for equilibrium. Similarly, the FS in FE simulation can be defined as the soil peak shear strength divided by the mobilised soil shear strength, which is equivalent to the inverse of the soil stress level S defined in this study. Because the FS obtained by the limit equilibrium method is an average value for the entire failure surface, the FS values obtained in FE analysis are also averaged along the failure surface, for comparison purposes.

Figure 18 shows the FS obtained by two different methods applied in Model M1. The FS predicted by both methods decreases as the g-level increases, but the FS predicted by the limit equilibrium method at each g-level increment exceeds that obtained by the FE method. This suggests that the limit equilibrium method tends to overestimate the FS or underestimate the developed stress level S, because the reinforcement loads in the limit equilibrium analysis in this study are input as constant values (i.e. ultimate tensile strength), and do not change with loading increment. That is, the reinforcement loads are assumed to be fully mobilised at the start of the limit equilibrium calculation; in practice, however, the mobilisation of reinforcement loads increases gradually with each g-level increment, as shown in the FE results. Therefore the FS predicted by the limit equilibrium method at each g-level increment has a higher value, because the analysis assigns higher values to the reinforcement loads than are actually mobilised in the centrifuge models. Although the FS calculated by the limit equilibrium method provides an indicator of slope stability, FE analysis using actual mobilised reinforcement loads arguably obtains FS calculations that provide a more realistic representation of the mobilisation of soil strength.

6. CONCLUSIONS

Numerical simulations were performed to investigate the distribution and development of backfill stresses and reinforcement tensile loads within GRS slopes. The results of

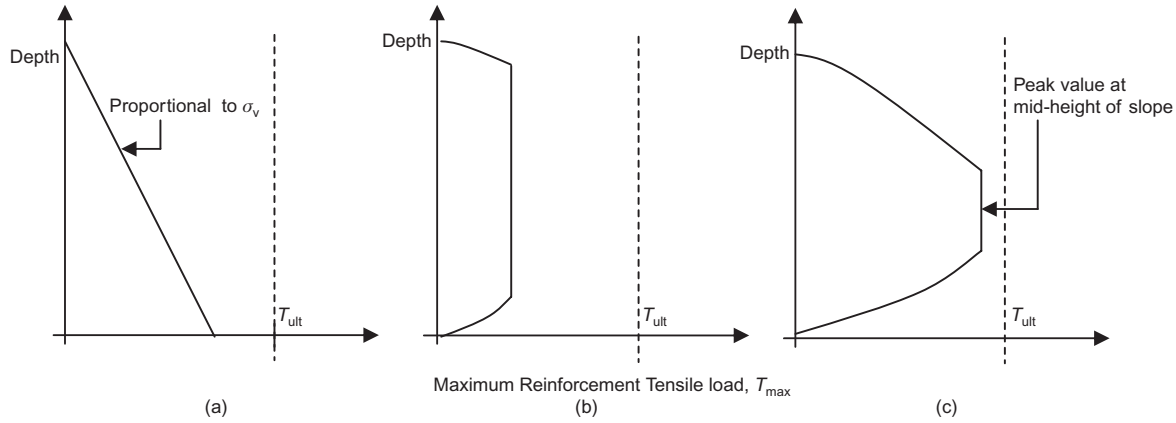

Figure 17. Distributions of maximum reinforcement tensile loads with depth: (a) triangular distribution assumed in current design methods; (b) uniform shape for working stress conditions; (c) trapezoidal shape for large soil strain conditions

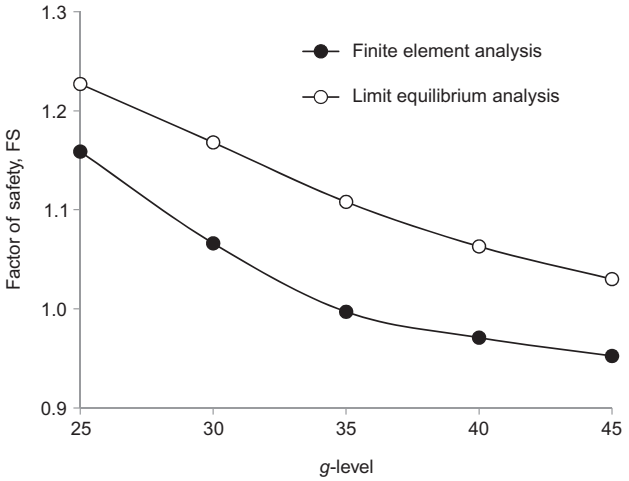

Figure 18. Comparison of FS obtained by finite element and limit equilibrium analyses in Model M1

this study provide the following insights into the behaviour and design of GRS structures.

- In both slope models constructed in this study, backfill stress increases with load and propagates along the potential failure surface. The stress level reaches peak ($S = 1$), and strength softening is initiated immediately at the top and toe of the slope at approximately FS = 1.2. Softening then occurs randomly and irregularly along the failure surface. The completed linkage of the soil-softening band throughout the entire potential failure surface occurs at approximately FS = 1.1.
- Mobilisation of soil stress was non-uniform along the failure surface. This finding contradicts current methods of analysing the internal stability of GRS structures, which assume that the soil shear strength along the failure surface mobilises equally, and reaches peak shear strength simultaneously.
- Numerical results suggest that using FS $\geqslant$ 1.3 for the global stability of a GRS slope provides a good criterion for ensuring the serviceability of slopes (i.e. the developed soil stress state is under work stress conditions).
- The failure surface corresponds to the locus of intense soil strains and the peak reinforcement tensions at each layer. Owing to the dilatancy of frictional materials, the soil horizontal strain along the failure surface is under tension. The slope settlement rate also increases significantly at the initiation of soil softening.
- The numerical results show that the initiation of soil softening and the failure of the slope occurred earlier in the slope model with low backfill density. A numerical explanation can be obtained by modelling soils with different densities by different sizes of peak failure envelope to represent different peak shear strengths. The numerical results support the view that peak shear strength, not residual shear strength, governs system stability.
- The mobilisation of reinforcement tensile loads within GRS slopes does not increase proportionally with loading increments. The reinforcement tensile loads do not mobilise significantly until the soil reaches its peak shear strength. Also, the distribution of maximum reinforcement tensile loads with depth is highly uniform at low *g*-levels and trapezoidal at high *g*-levels. The peak value is located at approximately the mid-height of the reinforced slopes. This observation contradicts the triangular distribution with depth assumed in current design methodologies for geosynthetic structures.
- The limit equilibrium analysis overestimates the FSs at each loading increment, compared with those obtained by finite element analysis. The use of actual mobilised reinforcement loads in finite element analysis provides a more realistic calculation of the FS used to represent mobilisation of soil strength.

Finally, this study did not evaluate the effects of compaction, reinforcement type or facing element on the distribution and development of soil stresses and reinforcement tensile loads. Further studies are needed to elucidate these effects.

ACKNOWLEDGEMENTS

The authors would like to thank the National Science Council of the Republic of China, Taiwan, for partially supporting this research under Grant No. NSC99-2218-E-001-006. The authors also sincerely appreciate the constructive criticism and comments by the anonymous reviewers.

NOTATION

Basic SI units are given in parentheses.

A original softening model variable in Lade–Kim model (dimensionless)
a modified softening model parameter (dimensionless)
a' failure criterion parameter in Lade–Kim model (dimensionless)
B original softening model variable in Lade–Kim model (dimensionless)
b modified softening model parameter (dimensionless)
C hardening model parameter in Lade–Kim model (dimensionless)
C_1 non-linear reinforcement model parameter (dimensionless)
C_2 non-linear reinforcement model parameter (dimensionless)
c modified softening model variable (dimensionless)
D_r relative density of backfill (dimensionless)
FS factor of safety (dimensionless)
f_n current failure envelope in Lade–Kim model (dimensionless)
f''_p size of yield surface (dimensionless)
f''_{pr} size of residual yield surface (dimensionless)
$(f''_p)_{S=1}$ size of yield surface at $S = 1$ (dimensionless)
h yield criterion parameter in Lade–Kim model (dimensionless)
M elastic model parameter in Lade–Kim model (dimensionless)
m failure criterion parameter in Lade–Kim model (dimensionless)
p hardening model parameter in Lade–Kim model (dimensionless)
p_a atmospheric pressure (Pa)
S soil stress level (dimensionless)
T reinforcement tensile load (N/m)
$T_{confined}$ mobilised confined tensile load (N/m)
T_{max} maximum reinforcement tensile load (N/m)
$T_{ult\_confined}$ ultimate confined tensile strength of reinforcement (N/m)
$T_{ult\_unconfined}$ ultimate unconfined tensile strength of reinforcement from wide-width test (N/m)
$T_{unconfined}$ mobilised unconfined tensile load (N/m)
W_p plastic work (Pa)
$(W_p/p_a)_{S=1}$ normalised plastic work at $S = 1$ (dimensionless)
α yield criterion parameter in Lade–Kim model (dimensionless)
γ unit weight of soil (N/m^3)
ε reinforcement tensile strain (dimensionless)
ε_x soil horizontal strain (dimensionless)
ε_y soil vertical strain (dimensionless)
η_1 peak failure criterion in Lade–Kim model (dimensionless)
τ_{oct} soil shear strain in octahedral plane (dimensionless)
ϕ_{ps} peak plane-strain soil fiction angle (degrees)
ϕ_{tc} peak soil fiction angle from under triaxial compression test (degrees)
λ elastic model parameter in Lade–Kim model (dimensionless)
μ plastic potential model parameter in Lade–Kim model (dimensionless)
ν Poisson's ratio (dimensionless)
Ψ_2 plastic potential model parameter in Lade–Kim model (dimensionless)

REFERENCES

AASHTO (2002). *Standard Specifications for Highway Bridges*, 17th edn, American Association of State Highway and Transportation Officials, Washington, DC, USA, 689 pp.

Allen, T. M. & Bathurst, R. J. (2002a). Soil reinforcement loads in geosynthetic walls at working stress conditions. *Geosynthetics International*, **9**, No. 5–6, 525–566.

Allen, T. M. & Bathurst, R. J. (2002b). Observed long-term performance of geosynthetic walls, and implications for design. *Geosynthetics International*, **9**, No. 5–6, 567–606.

Allen, T. M., Bathurst, R. J., Holtz, R. D., Walters, D. & Lee Wei, F. (2003). A new working stress method for prediction of reinforcement loads in geosynthetic walls. *Canadian Geotechnical Journal*, **40**, No. 5, 976–994.

Arriaga, F. (2003). *Response of Geosynthetic-Reinforced Structures under Working Stress and Failure Conditions*, PhD dissertation, Department of Civil Engineering, University of Colorado, Boulder, CO, USA.

Bathurst, R. J. (1993). Investigation of footing restraint on stability of large-scale reinforced soil wall tests. *Proceedings of the 46th Canadian Geotechnical Conference*, Saskatoon, Saskatchewan, pp. 389–398.

Bathurst, R. J., Miyata, Y., Nernheim, A. & Allen, T. M. (2008). Refinement of *K*-stiffness method for geosynthetic reinforced soil walls. *Geosynthetics International*, **15**, No. 4, 269–295.

Ballegeer, J. P. & Wu, J. T. H. (1993). Intrinsic confined and unconfined load-deformation properties of geotextiles. *Geosynthetic Soil Reinforcement Testing Procedures*, ASTM STP 1190, S. C. J. Cheng, Editor, American Society for Testing and Materials, Philadelphia, PA, pp. 16–31.

Elias, V., Christopher, B. R. & Berg, R. R. (2001). *Mechanically Stabilized Earth Walls and Reinforced Soil Slopes Design and Construction Guidelines*, Report No. FHWA-NHI-00-043, National Highway Institute, Federal Highway Administration, Washington, DC, March,

Hatami, K. & Bathurst, R. J. (2005). Development and verification of a numerical model for the analysis of geosynthetic-reinforced soil segmental walls under working stress conditions. *Canadian Geotechnical Journal*, **67**, No. 4, 1066–1085.

Hatami, K. & Bathurst, R. J. (2006). Numerical model for reinforced soil segmental walls under surcharge loading. *Journal of Geotechnical and Geoenvironmental Engineering, ASCE*, **132**, No. 6, 673–684.

Jakobsen, K. P. & Lade, P. V. (2002). Implementation algorithm for a single hardening constitutive model for frictional materials. *International Journal for Numerical and Analytical Methods in Geomechanics*, **26**, No. 7, 661–681.

Karpurapu, R. G. & Bathurst, R. J. (1995). Behaviour of geosynthetic reinforced soil retaining walls using the finite element method. *Computers and Geotechnics*, **17**, No. 3, 279–299.

Kim, M. K. & Lade, P. V. (1988). Single hardening constitutive model for frictional materials. I: Plastic potential function. *Computers and Geomechanics*, **5**, No. 4, 307–324.

Lade, P. V. & Jakobsen, K. P. (2002). Incrementalization of a single hardening constitutive model for frictional materials. *International Journal for Numerical and Analytical Methods in Geomechanics*, **26**, No. 7, 647–659.

Lade, P. V. & Kim, M. K. (1988a). Single hardening constitutive model for frictional materials. II: Yield criterion and plastic work contours. *Computers and Geomechanics*, **6**, No. 1, 13–29.

Lade, P. V. & Kim, M. K. (1988b). Single hardening constitutive model for frictional materials. III: Comparisons with experimental data. *Computers and Geomechanics*, **6**, No. 1, 31–47.

Lade, P. V. & Kim, M. K. (1995). Single hardening constitutive model for soil, rock and concrete. *International Journal of Solids and Structures*, **32**, No. 14, 1963–1978.

Leshchinsky, D. (2001). Design dilemma: use peak or residual strength of soil. *Geotextiles and Geomembranes*, **19**, No. 2, 111–125.

Leshchinsky, D. & Field, D. A. (1987). Soil load elongation, tensile strength and interface friction angle of nonwoven geotextiles. *Geosynthetics '87*, New Orleans, LA, USA, pp. 238–249.

Ling, H. I., Wu, J. T. H. & Tatsuoka, F. (1992). Short-term strength and deformation characteristics of geotextiles under typical operational conditions. *Geotextiles and Geomembranes*, **11**, No. 2, 185–219.

Montalvo, J. R. & Sickler, W. (1993). Comparison of geotextiles: the correlation between test methods and practical performance. *Proceedings of the Geosynthetics 93 Conference*, Vancouver, Canada, pp. 547–559.

NCMA (2010). *Design Manual for Segmental Retaining Walls*, 3rd edn, Collin, J., Editor, National Concrete Masonry Association, Herndon, VA, USA.

Spencer, E. (1967). A method of analysis of the stability of embankments assuming parallel inter-slice forces. *Géotechnique*, **24**, No. 4, 661–665.

Suzuki, K. & Yamada, T. (2006). Double strain softening and diagonally crossing shear bands of sand in drained triaxial tests. *International Journal of Geomechanics*, **6**, No. 6, 440–446.

Wu, J. T. H. (1991). Measuring inherent load-extension properties of geotextiles for design of reinforced structures. *Geotechnical Testing Journal*, **14**, No. 2, 157–165.

Yang, K.-H. (2009). *Stress Distribution within Geosynthetic-Reinforced Soil Structures*, PhD dissertation, Department of Civil, Architectural and Environmental Engineering, The University of Texas at Austin, USA.

Yoshida, T. & Tatsuoka, F. (1997). Deformation property of shear band in sand subjected to plane strain compression and its relation to particle characteristics. *Proceedings of the 14th International Conference on Soil Mechanics and Foundation Engineering*, Hamburg, Germany, pp. 237–240.

Yoshida, T., Tatsuoka, F., Siddiquee, M. S. A. & Kamegai, Y. (1993). Shear banding in sands in plane strain compression. *Proceedings of the 3rd International Workshop on Localisation and Bifurcation Theory for Soils and Rocks*, Grenoble, France, pp. 165–179.

Zornberg, J. G. (1994). *Performance of Geotextile Reinforced Soil Structures*, PhD dissertation, Department of Civil Engineering, University of California, Berkeley, CA, USA.

Zornberg, J. G. (2002a). Peak versus residual shear strength in geosynthetic-reinforced soil design. *Geosynthetics International*, **9**, No. 4, 301–318.

Zornberg, J. G. (2002b). Peak versus residual shear strength in geosynthetic-reinforced soil design: discussion and response 1. *Geosynthetics International*, **9**, No. 4, 381–386.

Zornberg, J. G. (2002c). Peak versus residual shear strength in geosynthetic-reinforced soil design: discussion and response 2. *Geosynthetics International*, **9**, No. 4, 387–390.

Zornberg, J. G. (2002d). Peak versus residual shear strength in geosynthetic-reinforced soil design: discussion and response 3. *Geosynthetics International*, **9**, No. 4, 391–393.

Zornberg, J. G. (2003). Peak versus residual shear strength in geosynthetic-reinforced soil design: discussion and response 4. *Geosynthetics International*, **10**, No. 6, 234–237.

Zornberg, J. G. & Arriaga, F. (2003). Strain distribution within geosynthetic-reinforced slopes. *Journal of Geotechnical and Geoenvironmental Engineering, ASCE*, **131**, No. 2, 141–150.

Zornberg, J. G. & Leshchinsky, D. (2001). Comparison of international design criteria for geosynthetic-reinforced soil structures. *Geosynthetics and Earth Reinforcement*, ISSMGE-TC9 report, Ochiai, H., Otani, J. and Miyata, Y., Editors, pp. 106–117.

Zornberg, J. G., Sitar, N. & Mitchell, J. K. (1998a). Performance of geosynthetic reinforced slopes at failure. *Journal of Geotechnical and Geoenvironmental Engineering, ASCE*, **124**, No. 8, 670–682.

Zornberg, J. G., Sitar, N. & Mitchell, J. K. (1998b). Limit equilibrium as basis for design of geosynthetic reinforced slopes. *Journal of Geotechnical and Geoenvironmental Engineering, ASCE*, **124**, No. 8, 684–698.

The Editor welcomes discussion on all papers published in Geosynthetics International. Please email your contribution to discussion@geosynthetics-international.com by 15 August 2012.